

Water Resources Research

TECHNICAL REPORTS: METHODS

10.1029/2020WR029361

Key Points:

- An experimental set-up for reliable pressure measurement in microfluidic cells during continuous enzyme-induced calcite precipitation
- Synchronized time-resolved optical microscopy with pressure measurements allows for correlating the pore space alteration with permeability
- X-ray microcomputed tomography complements optical microscopy for estimating volume changes

Supporting Information:

- Supporting Information S1

Correspondence to:

F. Weinhardt,
felix.weinhardt@iws.uni-stuttgart.de

Citation:

Weinhardt, F., Class, H., Vahid Dastjerdi, S., Karadimitriou, N., Lee, D., & Steeb, H. (2021). Experimental methods and imaging for enzymatically induced calcite precipitation in a microfluidic cell. *Water Resources Research*, 57, e2020WR029361. <https://doi.org/10.1029/2020WR029361>

Received 21 DEC 2020

Accepted 29 JAN 2021

© 2021. The Authors.

This is an open access article under the terms of the [Creative Commons Attribution License](#), which permits use, distribution and reproduction in any medium, provided the original work is properly cited.

Experimental Methods and Imaging for Enzymatically Induced Calcite Precipitation in a Microfluidic Cell

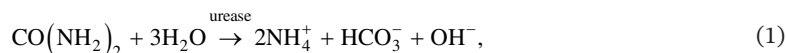
Felix Weinhardt¹ , Holger Class¹ , Samaneh Vahid Dastjerdi² , Nikolaos Karadimitriou² , Dongwon Lee² , and Holger Steeb^{2,3} 

¹Department of Hydromechanics and Modelling of Hydrosystems, University of Stuttgart, Stuttgart, Germany, ²Institute of Applied Mechanics, University of Stuttgart, Stuttgart, Germany, ³SC SimTech, University of Stuttgart, Stuttgart, Germany

Abstract Enzymatically induced calcite precipitation (EICP) in porous media can be used as an engineering option to achieve precipitation in the pore space, for example, aiming at a targeted sealing of existing flow paths. This is accomplished through a porosity and consequent permeability alteration. A major source of uncertainty in modeling EICP is in the quantitative description of permeability alteration due to precipitation. This report presents methods for investigating experimentally the time-resolved effects of growing precipitates on porosity and permeability on the pore scale, in a poly-di-methyl-siloxane microfluidic flow cell. These methods include the design and production of the microfluidic cells, the preparation and usage of the chemical solutions, the injection strategy, and the monitoring of pressure drops for given fluxes for the determination of permeability. EICP imaging methods are explained, including optical microscopy and X-ray microcomputed tomography (XRCT), and the corresponding image processing and analysis. We present and discuss a new experimental procedure using a microfluidic cell, as well as the general perspectives for further experimental and numerical simulation studies on induced calcite precipitation. The results of this study show the enormous benefits and insights achieved by combining both light microscopy and XRCT with hydraulic measurements in microfluidic chips. This allows for a quantitative analysis of the evolution of precipitates with respect to their size and shape, while monitoring their influence on permeability. We consider this to be an improvement of the existing methods in the literature regarding the interpretation of recorded data (pressure, flux, and visualization) during pore morphology alteration.

1. Introduction

Induced calcite precipitation is an engineering option which can be employed for a targeted sealing of flow paths in the subsurface as it might be necessary in geological gas storage in the presence of conductive faults (Ebigbo et al., 2010; Hommel et al., 2013; Phillips, Gerlach, et al., 2013; Phillips, Lauchnor, et al., 2013), for creating barriers for groundwater and containment of subsurface contamination (Cuthbert et al., 2013), and for soil stabilization and improvement of the mechanical soil properties (Hamdan & Kavazanjian, 2016; van Paassen et al., 2010; Wiffin et al., 2007). There are different techniques to achieve targeted calcite precipitation at a desired location. One of them is referred to as enzymatically induced calcite precipitation (EICP). Basically, EICP as we employ it here, relies on the dissociation of urea into carbon dioxide and ammonium catalyzed by the enzyme urease, which is extracted from jack-bean meal (JBM). In circumneutral environments regarding the pH value, ammonium (NH_4^+) and bicarbonate are the dominant products of hydrolysis, see Equation 1 (Mitchell et al., 2019). However, carbon dioxide in aqueous solutions occurs as carbonic acid (H_2CO_3), bicarbonate (HCO_3^-), or carbonate (CO_3^{2-}), depending on the pH value. Since ammonia acts as a weak base by taking up a proton and producing hydroxide, it increases the pH value and shifts the equilibrium toward carbonate ions. The additional presence of calcium ions, in our case provided by adding calcium chloride, forces calcium carbonate to precipitate. According to van Paassen (2009), the release of a proton (H^+) during the calcium carbonate precipitation buffers the production of hydroxide during the hydrolysis, see Equation 2. On the pore scale, precipitated calcium carbonate leads to changes in pore morphology, and on a larger scale, after averaging, this corresponds to changes in the effective quantities porosity and permeability,



In contrast to EICP, the technology of microbially induced calcite precipitation (MICP) relies on microbes expressing the enzyme urease. While the basic mechanism of precipitating carbonates altering the pore morphology is similar as in EICP, the MICP technology is more complex in application; and in particular, the impacts on porous-media properties are even more challenging to model. MICP involves the growth of bacteria and biofilms that have also an influence on the evolving pore space, however not the same as the precipitated calcite. Biofilm is a soft matter and to some extent flexible to adapt to variable shear stress at variable flow velocity. In contrast, precipitated carbonates tend to be more rigid solids.

Recent models developed for MICP have focused on the reaction part and its kinetics (Bachmeier et al., 2012; Ebigbo et al., 2010; Hommel et al., 2015), while it is acknowledged that kinetics are often strongly coupled to hydraulic processes (Ebigbo et al., 2012; Hommel et al., 2016). It has been shown that MICP models can be successfully applied to field-scale application (Cunningham et al., 2019; Minto et al., 2019), although it is highly challenging to validate such models with appropriate and relevant experiments.

In this study, we aim at elaborating on the much-needed experimental evidence for a deeper understanding of the processes at the pore scale that alter pore morphology and eventually change effective parameters porosity and permeability. We envision to determine more thorough process-related knowledge on porosity–permeability relations regarding EICP and MICP. We acknowledge that the Darcy scale (or REV scale), see for example, the respective definitions in Hommel et al. (2018), is the appropriate scale to model field-scale applications of MICP or EICP, where computational demands can become a limiting factor. However, it is the pore scale where the morphological changes occur and from where we, consequently, need to derive new insights. Therefore, we use microfluidics for analyzing EICP processes in the details of our interest.

Precipitation processes in microfluidic devices have been studied in the past with various objectives. In the work of Zhang et al. (2010), mixing-induced carbonate precipitation was investigated in a microfluidic cell made out of Pyrex glass and silicon with the dimensions of 2 cm × 1 cm. The process was observed by optical microscopy with a resolution of 1.62 and 0.65 μm/pixel. Yoon et al. (2012) performed pore-scale simulations based on these experiments. Wang et al. (2019) studied MICP in a microfluidic chip made out of poly-di-methyl-siloxane (PDMS) with the dimension of 1.5 cm × 1.5 cm, fabricated very similar compared to the one that is used here. With a very high resolution of 0.65 μm/pixel, they were able to observe bacteria, as well as to capture qualitatively the shape of single crystals. In contrast, the experiments of Kim et al. (2020) were performed on a larger scale, observing the whole microfluidic chip over time with a resolution of 6.5 μm/pixel, during sequential injections of reactive solutions for EICP. The microfluidic chip was made out of glass and had the dimensions of 2.1 × 1.3 cm. Based on image processing, statistical analysis of the precipitates, more precisely the size distribution over time, was conducted and compared to a simplified kinetic model.

As already mentioned above, it is very important to get reliable quantitative information on the change of pore volume, that is, porosity on the Darcy scale, and on the alteration of pore morphology. Optical microscopy and image processing can provide mainly 2D information with limited details in the through-plane direction. As a complement to optical microscopy, we used X-ray microcomputed tomography (XRCT) to acquire information also in the through-plane direction, with our primary focus being on the change in the hydraulic parameters, like permeability, due to the growth of precipitates. Therefore, it is necessary to be able to monitor the induced pressure drop across the flow network reliably, under various boundary-flow conditions. The experiments presented here combine the visual observation of crystal nucleation and growth over time with reliable pressure measurements under continuous flow conditions. We use XRCT analysis of the shape of the crystals in order to be able to correlate 2D images with 3D structures of the precipitated carbonates in an effective way. This new experimental approach that we present here will allow for more comprehensive studies on EICP, and perspective also on MICP, and its particularly complex porosity–permeability relations.

Furthermore, the results presented here can serve as a database for a comparison study of reactive transport simulations on the pore scale, including calcite precipitation.

Below, we introduce the materials and methods that are used, developed, and applied. This includes the production of the microfluidic cells by soft lithography, the experimental procedures for the EICP studies, as well as the imaging techniques. Subsequently, we present exemplary results on permeability determination from experiments and evaluate the imaging techniques. The discussion of the results puts a focus on the development of methods and on a workflow that is adapted to the EICP application. Still, we are able to draw important conclusions for further studies toward a better understanding of porosity–permeability relations in porous media affected by EICP or MICP.

2. Materials and Methods

The set-up and the workflow of the microfluidic experiment, including the preparation of the chemical solutions, are described in detail below. Subsequently, the two imaging methods, optical microscopy and XRCT scanning, are described and the corresponding postprocessing of the images is explained.

2.1. Microfluidic Experiments

In the scope of this work, three experiments were conducted, in the following referred to as Experiments 1–3. For each experiment, one microfluidic cell was produced, based on the same design. Essentially, they are three repetitions of identical experimental conditions, except for Experiment 2, which was cut short since clogging occurred during the precipitation. The set-up, experimental procedure, and image processing are explained in the following.

The microfluidic cells were produced by following the regular workflow of soft lithography (Karadimitriou et al., 2013; Xia & Whitesides, 1998). The designs of the pore-network geometry were generated with AutoCAD[®] and subsequently printed on an A4 transparency, with the pore space being transparent and the solid space being opaque. Such a transparency is commonly called a mask. These masks are employed in optical lithography with the use of SU8-2100 photoresist to produce photoresist spin-coated silicon wafers. After having followed the regular steps of photolithography, the photoresist features sticking out of the wafer had a height of 85 μm . These wafers were used in the production process of the actual microfluidic cells out of PDMS. A mixture of Dow Corning SYLGARD[®] 184 Silicone Elastomer base and the curing agent, at a mixing ratio of 10:1, is poured into a petri dish with a wafer, so as to create the PDMS slab with the features of the flow network. An equal quantity of the mixture is also poured into another petri dish without a wafer, to create a blank slab which is used as the sealing one. After degassing and subsequent curing for 2 h at 68°C, the resulting PDMS slabs are carefully removed from the wafer and the petri dish. Holes ($\varnothing 1.5$ mm) for the inlet and outlet tubes are punched and the PDMS slabs are diced to fit the size of a standard glass slide for microscopy (26 mm \times 76 mm). The bonding of the two PDMS slabs together and subsequently on a glass slide is done with the corona treatment described in Haubert et al. (2006). After another 24 h, the bonding is complete and the microfluidic cells are ready to be used in the experiments.

The reactive solutions were prepared as follows: Solution 1 contained 1 g urea with a molar mass of 60.06 $\frac{\text{g}}{\text{mol}}$ and 2.45 g calcium chloride dihydrate with a molar mass of 147 $\frac{\text{g}}{\text{mol}}$ mixed in 50 mL deionized water. The mass concentrations correspond to an equimolar concentration of $1/3 \frac{\text{mol}}{\text{L}}$. Both chemicals were provided by MERCK[®]. For Solution 2, the enzyme urease is extracted from JBM provided by Sigma Aldrich[®]. JBM (0.25 g) together with 50 mL deionized water are stirred at a constant temperature of 8°C. After 17 h of stirring, the solution is vacuum filtered twice with a 0.45 μm cellulose membrane to remove any JBM particles remaining. The concentrations we used to prepare the reactive solutions are based on similar investigations on EICP, like in the work of Kim et al. (2020) and Feder et al. (2020). From preliminary batch experiments, we know that right after mixing equal volumes of Solutions 1 and 2 the resulting pH value is around 7.

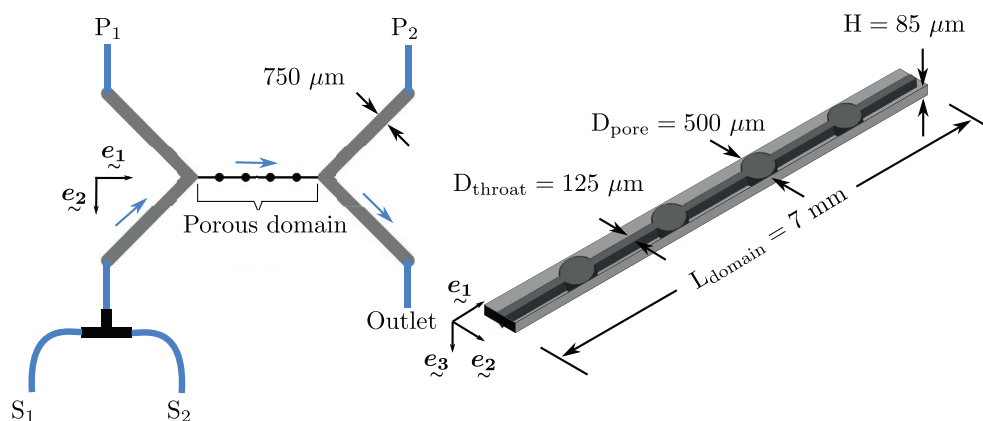


Figure 1. Left: sketch of the microfluidic set-up including the porous domain (black); the inlet, outlet, and pressure channels (gray); the tubes (blue) connected to the syringe pumps (S_1 and S_2) and to the pressure sensors (P_1 and P_2); the flux is indicated with blue arrows. Right: porous domain and its dimensions.

The design of the microfluidic cell and its geometrical parameters are shown in Figure 1. The pore throats have a size of $125\ \mu\text{m}$ and the pore bodies a diameter of $500\ \mu\text{m}$. This is comparable to the geometric features of previous studies, like in Wang et al. (2019) or Kim et al. (2020) where the size of the pore throats range from below 50 to $140\ \mu\text{m}$. The inlet at the bottom left is connected with two $2.5\ \text{mL}$ glass syringes (S_1 , S_2) guided by two, one for each, midpressure pumps CETONI neMESYS 100 N which generate the flow. The interface between the syringe pumps and a computer for the control of the whole process is a base module, CETONI BASE 120. The software QMixElements is used to operate the experiment via predefined scripts. The tubes, connecting the microfluidic cell with the syringes and the pressure sensors, have an inner diameter of $0.5\ \text{mm}$ and an outer diameter of $1.59\ \text{mm}$ ($1/16\ \text{in.}$) and are made of Teflon (poly-tetra-fluoro-ethylene). The outlet is connected to a reservoir with a constant water table of $10\ \text{cm}$ above the microfluidic cell. This induces a back-pressure in order to reduce the risk of bubble formation during the experiment. Air bubbles can lead to difficulties in image postprocessing, as shown in the work of Kim et al. (2020), and are likely to disturb the pressure measurements. The tubes for the outlet have an inner diameter of $0.75\ \text{mm}$ to avoid clogging. P_1 and P_2 indicate the location of the Elveflow MPS0 pressure sensors with a range of $70\ \text{mbar}$. The analog voltage signals of the pressure sensors are acquired and digitized with $16\ \text{bit}$ using the CETONI I/O module at a rate of $1\ \text{Hz}$. By design, the inlet and outlet geometry was chosen to be bigger, so that they would not strongly affect the evolution of events inside the pore structure.

The pressure sensors are connected in parallel to the inlet and outlet channels, making sure that the pressure measurements are always taken under no flow (static) conditions. The inlet channels are large enough to be hydraulically connected to the pressure sensor during the whole precipitation process. Thus, it is possible to measure the pressure drop of the domain of interest (top right in Figure 1) without being compromised by precipitates in the inlet and outlet channels of the microfluidic cell. The porous domain in this work is defined as shown in Figure 1 on the right. Note that permeability in this work is defined arbitrarily (with assumptions for the dimensions used in Darcy's law), since the objective of this work is to measure relative effects, and the value for permeability is only used as a normalization factor. The domain is a cuboid with dimensions $D_{\text{pore}} \times H \times L_{\text{domain}}$. Under the same concept, we only refer to porosity as "normalized porosity" due to the increased degrees of freedom in the selection of a reference domain.

Each experiment can be subdivided into three stages: (a) initial permeability measurement, (b) continuous injection of reactive solution, and (c) final permeability measurement, with the ambient temperature being 23°C .

In the beginning of the experiment, the permeability is estimated by applying different flow rates (0.01 – $1.5\ \frac{\mu\text{L}}{\text{s}}$) with deionized water only, and by measuring the pressure difference $\Delta p = p_2 - p_1$. Based on these measurements, the initial permeability of the porous domain can then be determined using Darcy's law

(Stage a). Afterward, the microfluidic cell is flushed with both reactant solutions at a high flow rate of $0.25 \frac{\mu\text{L}}{\text{s}}$ for 5 min. Urea–calcium-chloride solution is introduced from S_1 and urease solution from S_2 , in order to fully saturate the microfluidic cell with the reactive solution. Consequently, the continuous injection of reactive solution starts: a constant flow rate of $0.01 \frac{\mu\text{L}}{\text{s}}$ for each syringe is applied for up to 5 h, resulting in a total flow of $0.02 \frac{\mu\text{L}}{\text{s}}$ and a forced mixing of the reactants in the inlet tube right before entering the microfluidic cell (Stage b). During this stage, precipitation is taking place and the pressure is continuously monitored at the inlet and outlet of the microfluidic cell in order to quantify the hydraulic effects of the pore space alterations. The flow rate was chosen to ensure creeping flow conditions ($Re < 1$). The characteristic length, in the calculation of the Reynold's number, in this case is the height of cell H , since it is the smallest feature in the cell which makes it the dominant dimension. After precipitation, the system is flushed with deionized water at a constant flow rate of $0.02 \frac{\mu\text{L}}{\text{s}}$ for 20 min. Finally, another permeability estimation is conducted by applying flow rates from 0.005 to $0.03 \frac{\mu\text{L}}{\text{s}}$ with water only, while measuring the induced pressure difference $\Delta p = p_2 - p_1$ (Stage c).

2.2. Imaging

During the experiments, the processes were observed using optical microscopy, and after the experiment the microfluidic cells underwent an XRCT scan with all the precipitates in place. The set-up and the subsequent image processing of these methods are described in detail in the following.

2.2.1. Optical Microscopy

The transparent nature of PDMS allows for the direct, real-time visualization of the processes taking place in the pore space by using transmitted light microscopy. For this purpose, a custom-made microscope has been developed, which is able to visualize samples with a resolution of $0.5\text{--}20 \mu\text{m}$ per camera pixel. In the Supporting Information, a sketch with all components is given. An extended version of this optical set-up can be found in Karadimitriou et al. (2012).

In order to analyze the images obtained from optical microscopy with respect to the porosity change and the crystal growth, the gray-scale images were processed with the software Matlab R2019b[®] (The Mathworks, Inc.) using a procedure briefly described in the following and illustrated in Figure S3. As a first step, a mask was created that defines the porous domain based on the initial image without any precipitates. This includes filtering, geometrical and morphological operations, and binarization methods. When comparing images at different time steps while precipitation is still taking place, it is important that they are geometrically aligned. Even though the set-up, including the stage and the camera, is fixed, small changes of the position can occur. To overcome this issue, all subsequent images are registered to the initial image, before applying the above-mentioned methods to them. In the resulting binarized images, individual crystal aggregates can be identified and the size of their 2D projection can be derived.

2.2.2. X-Ray Microcomputed Tomography

After the EICP experiment, the microfluidic cells were further investigated by means of XRCT imaging. The scan was performed in an open and modular XRCT device. More details about the set-up can be found in the work of Ruf and Steeb (2020) or in the supporting information. The microfluidic cell domain was cut out from the total 3D-scanned volume. With the resolution of $4.25 \frac{\mu\text{m}}{\text{px}}$, the size of the XRCT-imaged area (after alignment) is $2,100 \times 519 \times 20$ voxels in length, width, and depth of the porous domain, respectively. This corresponds to a domain volume of approximately $89 \times 22 \times 0.085 \text{ mm}$.

XRCT scanning was carried out for all three experiments. However, due to the vast amount of a second phase observed around the precipitates after the experiments and before the scans, which will be explained in Section 3.3, only the XRCT data set of Experiment 3 was further postprocessed.

Image processing was performed again by using Matlab R2019b[®] (The Mathworks, Inc.). The raw images were imported to Matlab as a 3D data set. For facilitating the comparison with the 2D information, the images were transformed to achieve a 3D data set, in which the porous domain is aligned as it is in the microscopy images. Afterward, the images were filtered with a 3D median filter and segmented. Two methods, (i) of maximum entropy and (ii) Otsu (1979) thresholding, were applied to segment the images into four different phases, including the PDMS, the pore space, the calcium carbonate precipitates, and a liquid-resembling phase surrounding some of the crystals. The particles smaller than 10 voxels, which are mostly noise, were removed from the 3D precipitates. The remaining connected components, referred to as crystals, were then investigated. A more detailed description of the image processing can be found in supporting information.

3. Evaluation of the Methods

We evaluate and discuss here the methods described in the previous sections by means of the three experiments. At first, we describe the estimation of the permeability by evaluating the pressure measurements in comparison to the applied boundary-flow conditions. Subsequently, the potential of combining optical microscopy and XRCT scanning is pointed out.

3.1. Determination of Permeability

The permeability of the cell was determined (i) free from precipitates and (ii) with precipitates. It was estimated by applying various boundary-flow rates of deionized water while measuring the corresponding pressure drop (Stages a and c). By rearranging Darcy's law and using the slope of the negative pressure drop over the flow rate s_{pq} , the intrinsic permeability k can then be calculated as

$$k = \frac{\mu L_{\text{domain}}}{A s_{pq}}, \quad (3)$$

with A being the cross-sectional area ($H \times D_{\text{pore}}$) and L_{domain} the length of the domain as defined in Figure 1. For example, Figure 2 displays the measured negative pressure drop over the flow rate for Experiment 1. The applied flow rates in the case of the clean cells (before precipitation) show a wider range (up to 1.5 $\frac{\mu\text{L}}{\text{s}}$) in order to overcome the relatively larger error for small pressure drops. In the case of the cells with precipitates, the permeability is expected to be significantly reduced, thus inducing higher pressure drops for the same boundary-flow conditions. This allowed us to employ lower flow rates in our effort to avoid detachment of the precipitates due to increased shear stresses, while still being able to measure the corresponding pressures in a reliable way.

The boundary pressure is monitored continuously during the entire injection and precipitation period (Stage b). Under the reasonable assumption that the fluid viscosity remains constant throughout the duration of the experiment, the normalized permeability is the reciprocal of the normalized pressure drop ($k/k_0 = \Delta p_0/\Delta p$), while the subscript "0" corresponding to the initial state of the system, before any precipitation.

For both Experiments 1 and 3, the permeability reductions obtained from the subsequent permeability measurement (Stage c) were slightly higher compared to the last measurement during the continuous injection. We think the reason for this is the following. The solution with reactants in the inlet tube has to be flushed through the microfluidic cell before being able to continue with injecting water at different flow rates. This may result in further ongoing precipitation. Besides that, the injection of water could potentially mobilize small precipitates which are subsequently trapped at locations further downstream, as also reported in Mountassir et al. (2014). Since the microfluidic cell from Experiment 2 was apparently clogged, the subsequent permeability measurement could not be performed. However, since we determine the initial and final permeability by injection of water at different flow rates, we are confident that this allows for verifying the continuous pressure measurement during the precipitation phase. This experimental protocol demonstrates that the continuous pressure-monitoring strategy as explained here allows for reliable determination of permeability reductions of up to 3 orders of magnitude. Figure 2 shows the negative pressure drop of Experiments 1–3 during the precipitation process (Stage b) and, additionally, the permeability estimation of the initial and final states is given exemplarily for Experiment 1 (Stages a and c).

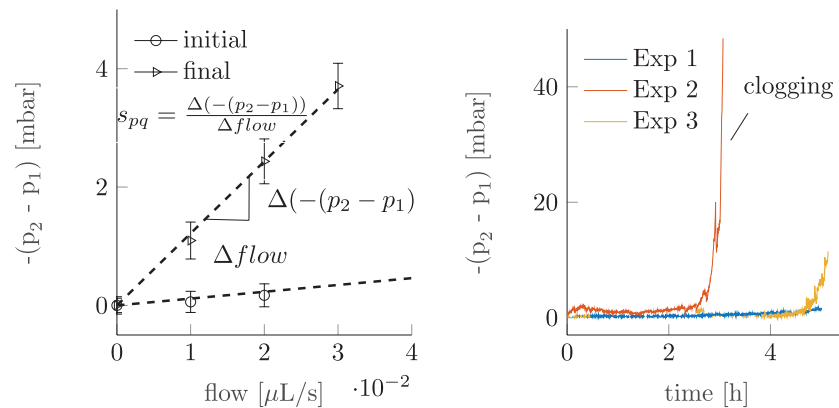


Figure 2. Left: negative pressure drop over flow rate for the cell at initial state and at the final state, after the precipitation—exemplary for Experiment 1; the slope s_{pq} is used to estimate the permeability based on Equation 3; right: negative pressure drop during the precipitation phase of Experiments 1–3.

3.2. Evolution Over Time as Derived From Optical Microscopy

The main advantage of using optical microscopy in this experimental procedure is the time-resolved visual observation of the precipitation process synchronized with continuous pressure measurements. This enables us to observe the nucleation and growth of the precipitates as well as their detachment and reattachment (if occurring) during the continuous injection of the reactant solutions. An exemplary detachment–reattachment process is shown in Figure S6.

After processing the images following the procedure in Section 2.2, the porosity change can be estimated, which is, in fact, essential for investigating porosity–permeability relations. Figure 3 shows the 2D porosity over time, normalized to its initial value. Experiments 1 and 2 show a similar trend of the reduction of the porosity over time, while in Experiment 3 the apparent decrease in pore volume is slower. Figure 3 shows that there are obviously less nuclei in the porous domain of Experiment 3. This lack of nucleation sites leads to a smaller decrease of the apparent 2D porosity over time. The nuclei seem to be spread randomly throughout the domain, but they could be influenced by small imperfections of the microfluidic cell itself. For example, small impurities of the elastomer base or curing agent, originating from the manufacturing process of the microfluidic cells, might cause these imperfections which can then result in a locally increased roughness of the surface. These imperfections can then act as initiation points and are, therefore, a preferred location for heterogeneous nucleation.

From 2D microscopy, we can easily observe crystal growth over time. However, the actual volume change including the third dimension can only be derived with further assumptions. In the work of Kim et al. (2020), the volume of individual crystals is estimated by assuming the shape of the crystals to be either cylindrical or semispherical. From the area observed by optical microscopy (A), an equivalent radius (r_{eq}) is calculated:

$$r_{eq} = \sqrt{\frac{A}{\pi}}. \quad (4)$$

The volume of individual crystals is then estimated based on the equivalent radius and the height of the microfluidic cell. However, in the work of Kim et al. (2020), the shapes are just hypothetical and have not been validated by three-dimensional imaging techniques. Following the same approach, other shapes like spherical or spheroidal shapes are potentially possible as well. In order to overcome these uncertainties, an additional XRCT scan has been performed in order to resolve the 3D structure of the precipitates.

3.3. 3D Structure of Precipitates Derived From XRCT Scan

In order to examine the shape of the crystal aggregates, the XRCT images are segmented and studied following the procedure as described in Section 2.2.2.

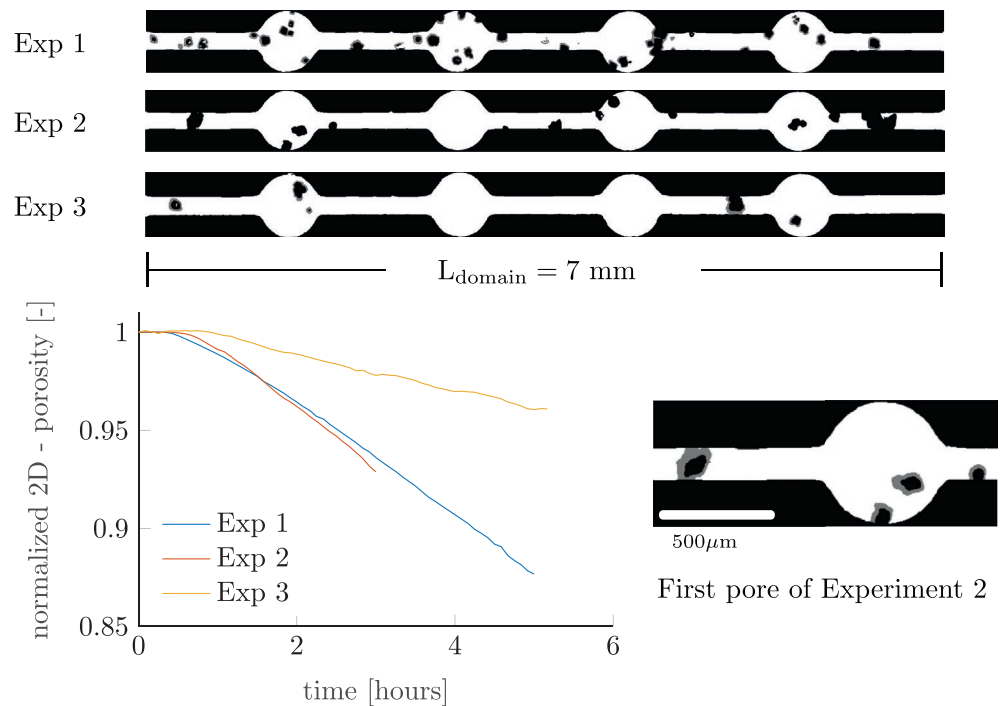


Figure 3. Top: processed images from optical microscopy of Experiments 1–3. Black indicates the crystals after 3 h and 10 min. Gray indicates the further development until the final states for Experiments 1 and 3; bottom left: normalized 2D porosity over time; right: crystal growth in the first pore of Experiment 2; gray indicates the growth within a period of 100 min.

One of the advantages of 3D imaging is the information it offers with respect to volume. Thus, the main purpose of performing an XRCT in this study is to support and complement the 2D information from optical microscopy imaging with the information on spatial extents in the third dimension. This is required for a reliable quantitative estimation of the porosity change in the 3D porous domain. For the figures from XRCT to be comparable to microscopy, the ideal case would be to preserve the final state of the crystals at the end of the experiments as accurately as possible.

After rinsing with deionized water and drying the cell when the experiment was concluded, it was observed that there was a second phase surrounding some of the precipitates. This phase had different X-ray attenuation properties, leading to distinctly different intensities of the gray values in the acquired images. In view of the fact that this second phase appears to be of unknown composition, we considered it not relevant for this work to further define its identity. Hence, in an attempt to be more compatible with the microscopy images, this second phase is removed from the XRCT data set. This is explained in more detail in the SI.

The investigation, with the focus being mainly on the shape-defining properties of the crystals, equipped us with the 3D structure of the crystal aggregates including their volume, surface, and distribution in the cell's depth. Figure 4 shows 2D projection of the microfluidic domain, including the shape of five crystal aggregates obtained from the XRCT scan, and demonstrates the opportunity that XRCT offers to determine the distribution of the aggregates in the depth of the cell. This information provides clues about the location of the nucleation point and to what extent they are attached to the walls of the flow cell as well. This is of great importance when studying EICP on the pore scale, since attachment and potential detachment of the aggregates strongly influence the process. Since we are able to resolve the 3D structure of the precipitates, we can use this to complement the optical imaging, for example, by evaluating different shape assumptions as mentioned in Section 3.2.

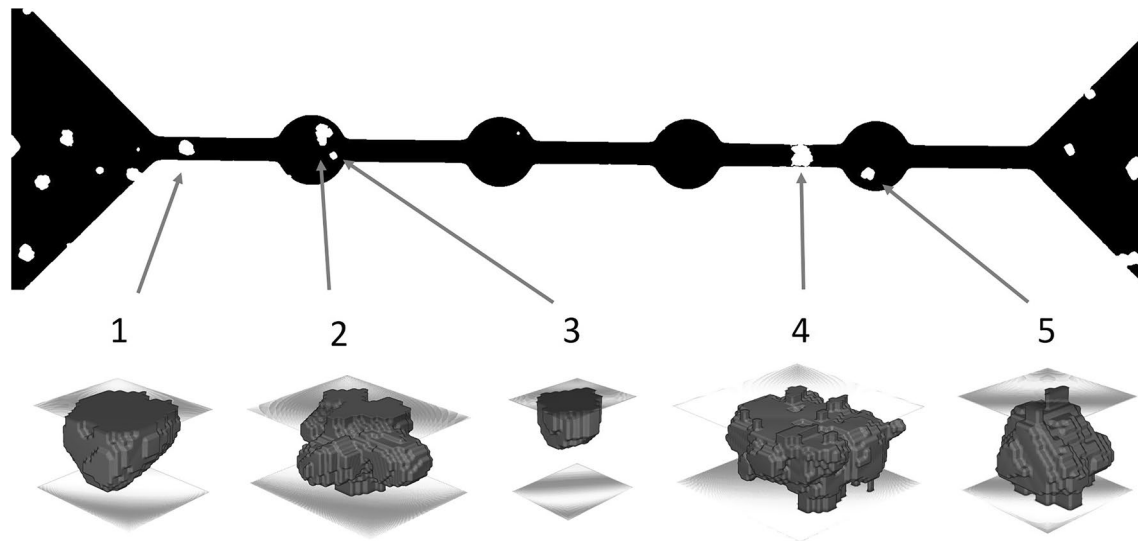


Figure 4. 2D projection of the microfluidic cell (top) and 3D structure of five crystal aggregates, obtained from the XRCT scan. XRCT, X-ray microcomputed tomography.

4. Discussion/Applicability for Further Investigations

As explained in Section 1, we consider this study being in the context of finding specific porosity–permeability relationships for EICP in porous media, and, perspectively, also for MICP where biofilms, additionally present in the pore space, render the problem even more complex. As a porous medium, we used flow cells made of PDMS, while we are aware of the possibility that the porous material and its surface may have an influence on the precipitation process, in particular on the generation of nucleation points due to locally increased roughness, surface charge, etc. This is definitely an aspect that we plan to consider in future studies.

What we have developed and presented above is an experimental strategy that we propose for assessing pore-scale alteration observed during EICP in microfluidic cells. We note here that the main achievement of this study is the experimental procedure rather than results for the envisioned porosity–permeability relations. The latter will be shown along with further experimental data and interpretations in a separate study. The requirements guiding us in designing the experimental procedure include a reliable determination of pore space alteration which can be resolved also in time. In other words, our demand is to assess the when, where, and what in the processes taking place regarding EICP with as much quantifiable data as possible. The cell design, the measurements, and the imaging techniques can be discussed in this context.

Regarding the design of the cell, we put an emphasis on a strongly simplified porous medium which allows for a detailed analysis of the shape of precipitated crystals. We note that this cell design due to its quasi-1D structure is probably not the best representative for deriving porosity–permeability relations in porous media. But the design is optimal for demonstrating and validating our workflow and, of course, it has to be changed and adapted to required complexities in future studies. Another important aspect for the cell design is the evaluation of pressure at the desired locations, that is, without being strongly influenced by precipitates in the inlet and outlet channels or tubes. With the designed pressure channels, we have found a satisfactory solution to this problem.

The continuous pressure measurements during injection and precipitation (Stage b) were necessary for the temporal resolution of the process. They were validated by permeability determination via injection of deionized water at varying rates, both before the injection (and precipitation) and after its stop. This implies a small temporal shift due to the required changes in the set-up, during which precipitation in the cell may go on and further change the pore space and the permeability. Yet, we could see that this effect is minor and the “validation” of the continuous pressure monitoring can be considered successful.

While the pressure information is important for concluding on permeability changes, imaging is the crucial part for the quantification of changes in pore morphology and pore volume. We have applied optical microscopy and, as a subsequent 3D characterization technique, XRCT scans. Similar to our approach with respect to the measurement of the pressure drop, we have here with the optical microscopy an approach of continuous monitoring during the injection and precipitation, while we use XRCT scans to prop up the 2D information from microscopy. Optical microscopy allows for observing changes of the pore structure synchronized with the continuous pressure measurements, but it does not resolve the structure of the precipitated solids in the third dimension.

We have mentioned that the microscopy images can be usefully complemented with the help of information from the XRCT scans. The XRCT scans, though costly and only a posteriori to perform unless maybe at a synchrotron tomography beamline, are able to resolve the third dimension. The shapes of the crystals can be examined and it enables finding reasonable approximations for volumes derived from 2D projections and, consequently, a better quantification of the changes in the pore space due to precipitation. This means that throughout our future experiments more value can be attributed to information from cheap and continuous optical microscopy. However, the XRCT scans require preparations; the cells need to be flushed, dried, and moved to the scanner. Thus, it is likely that there occur some discrepancies between the “final” state of the injection/precipitation experiment and scanned state. Time-resolved scanning during the experiment would require to apply for beam time in a synchrotron, which implies certain limitations. It is worth noting that the perfect experimental XRCT technique for a microfluidic cell, in which the aspect ratio of the depth relative to the other dimensions is small and is considered as flat, would be laminography (Gondrom et al., 1999). Nevertheless, we were able to derive beneficial information out of the XRCT set-up as it is already available to us.

The experimental procedure we propose in this study can be applied for more realistic designs of the porous domain, where flow has more degrees of freedom to bypass clogging, in order to derive realistic porosity–permeability relations. These relations are crucially important when modeling reactive transport during EICP or MICP including precipitation on the REV scale.

The provided data include the segmented XRCT scan, as well as the segmented images of microscopy. Based on these data, pore-scale simulations can be validated.

Data Availability Statement

The data sets will be available in the Data Repository of the University of Stuttgart (DaRUS). Two data sets are separately published: images of optical microscopy together with the log data, including flow rates and pressure measurements, can be found in Weinhardt et al. (2021). The XRCT data set is published in Vahid Dastjerdi et al. (2021).

Acknowledgments

The work was supported by the German Research Foundation (Deutsche Forschungsgemeinschaft, DFG) within the Collaborative Research Center 1313 (project number 327154368 – SFB 1313). We acknowledge funding by the DFG under Germany’s Excellence Strategy EXC 2075 (project number 390740016 - EXC 2075).

References

- Bachmeier, K., Williams, A., Warmington, J., & Bang, S. (2012). Urease activity in microbiologically-induced calcite precipitation. *Journal of Biotechnology*, 93, 171–181. [https://doi.org/10.1016/s0168-1656\(01\)00393-5](https://doi.org/10.1016/s0168-1656(01)00393-5)
- Cunningham, A., Class, H., Ebigo, A., Gerlach, R., Phillips, A., & Hommel, J. (2019). Field-scale modeling of microbially induced calcite precipitation. *Computational Geosciences*, 23, 399–414. <https://doi.org/10.1007/s10596-018-9797-6>
- Cuthbert, M., McMillan, L., Handley-Sidhu, S., Riley, M., Tobler, D., & Phoenix, V. (2013). A field and modeling study of fractured rock permeability reduction using microbially induced calcite precipitation. *Environmental Science & Technology*, 47(23), 13637–13643. <https://doi.org/10.1021/es402601g>
- Ebigo, A., Helmig, R., Cunningham, A., Class, H., & Gerlach, R. (2010). Modelling biofilm growth in the presence of carbon dioxide and water flow in the subsurface. *Advances in Water Resources*, 33(7), 762–781. <https://doi.org/10.1016/j.advwatres.2010.04.004>
- Ebigo, A., Phillips, A., Gerlach, R., Helmig, R., Cunningham, A., Class, H., & Spangler, L. (2012). Darcy-scale modeling of microbially induced carbonate mineral precipitation in sand columns. *Water Resources Research*, 48, W07519. <https://doi.org/10.1029/2011WR011714>
- Feder, M. J., Akyel, A., Morasko, V. J., Gerlach, R., & Phillips, A. J. (2020). Temperature-dependent inactivation and catalysis rates of plant-based ureases for engineered biomineralization. *Engineering Reports*, 3(2), e12299. <https://doi.org/10.1002/eng2.12299>
- Gondrom, S., Zhou, J., Maisl, M., Reiter, H., Kröning, M., & Arnold, W. (1999). X-ray computed laminography: An approach of computed tomography for applications with limited access. *Nuclear Engineering and Design*, 190, 141–147. [https://doi.org/10.1016/S0029-5493\(98\)00319-7](https://doi.org/10.1016/S0029-5493(98)00319-7)
- Hamdan, N., & Kavazanjian, E. (2016). Enzyme-induced carbonate mineral precipitation for fugitive dust control. *Géotechnique*, 66(7), 546–555. <https://doi.org/10.1680/jgeot.15.P.168>

- Haubert, K., Drier, T., & Beebe, D. (2006). PDMS bonding by means of a portable, low-cost corona system. *Lab on a Chip*, 6(12), 1548–1549. <https://doi.org/10.1039/b610567j>
- Hommel, J., Coltman, E., & Class, H. (2018). Porosity–permeability relations for evolving pore space: A review with a focus on (bio-)geochemically altered porous media. *Transport in Porous Media*, 124, 589–629. <https://doi.org/10.1007/s11242-018-1086-2>
- Hommel, J., Cunningham, A., Helmig, R., Ebigbo, A., & Class, H. (2013). Numerical investigation of microbially induced calcite precipitation as a leakage mitigation technology. *Energy Procedia*, 40C, 392–397. <https://doi.org/10.1016/j.egypro.2013.08.045>
- Hommel, J., Lauchnor, E., Gerlach, R., Cunningham, A., Ebigbo, A., Helmig, R., & Class, H. (2016). Investigating the influence of the initial biomass distribution and injection strategies on biofilm-mediated calcite precipitation in porous media. *Transport in Porous Media*, 114(2), 557–579. <https://doi.org/10.1007/s11242-015-0617-3>
- Hommel, J., Lauchnor, E., Phillips, A., Gerlach, R., Cunningham, A. B., Helmig, R., et al. (2015). A revised model for microbially induced calcite precipitation: Improvements and new insights based on recent experiments. *Water Resources Research*, 51, 3695–3715. <https://doi.org/10.1002/2014WR016503>
- Karadimitriou, N. K., Joekar-Niasar, V., Hassanizadeh, S. M., Kleingeld, P. J., & Pyrak-Nolte, L. J. (2012). A novel deep reactive ion etched (DRIE) glass micro-model for two-phase flow experiments. *Lab on a Chip*, 12, 3413–3418. <https://doi.org/10.1039/C2LC40530J>
- Karadimitriou, N. K., Musterd, M., Kleingeld, P. J., Kreutzer, M. T., Hassanizadeh, S. M., & Joekar-Niasar, V. (2013). On the fabrication of PDMS micromodels by rapid prototyping, and their use in two-phase flow studies. *Water Resources Research*, 49, 2056–2067. <https://doi.org/10.1002/wrcr.20196>
- Kim, D. H., Mahabadi, N., Jang, J., & van Paassen, L. A. (2020). Assessing the kinetics and pore-scale characteristics of biological calcium carbonate precipitation in porous media using a microfluidic chip experiment. *Water Resources Research*, 56, e2019WR025420. <https://doi.org/10.1029/2019WR025420>
- Minto, J. M., Lunn, R. J., & El Mountassir, G. (2019). Development of a reactive transport model for field-scale simulation of microbially induced carbonate precipitation. *Water Resources Research*, 55, 7229–7245. <https://doi.org/10.1029/2019WR025153>
- Mitchell, A. C., Espinosa-Ortiz, E. J., Parks, S. L., Phillips, A. J., Cunningham, A. B., & Gerlach, R. (2019). Kinetics of calcite precipitation by ureolytic bacteria under aerobic and anaerobic conditions. *Biogeosciences*, 16(10), 2147–2161. <https://doi.org/10.5194/bg-16-2147-2019>
- Mountassir, G. E., Lunn, R. J., Moir, H., & MacLachlan, E. (2014). Hydrodynamic coupling in microbially mediated fracture mineralization: Formation of self-organized groundwater flow channels. *Water Resources Research*, 50, 1–16. <https://doi.org/10.1002/2013WR013578>
- Otsu, N. (1979). A threshold selection method from gray-level histograms. *IEEE Transactions on Systems, Man, and Cybernetics*, 9(1), 62–66. <https://doi.org/10.1109/TSMC.1979.4310076>
- Phillips, A., Gerlach, R., Lauchnor, E., Mitchell, A., Cunningham, A., & Spangler, L. (2013). Engineered applications of ureolytic biomineralization: A review. *Biofouling*, 29(6), 715–733. <https://doi.org/10.1080/08927014.2013.796550>
- Phillips, A., Lauchnor, E., Eldring, J., Esposito, R., Mitchell, A., Gerlach, R., et al. (2013). Potential CO₂ leakage reduction through biofilm-induced calcium carbonate precipitation. *Environmental Science & Technology*, 47(1), 142–149. <https://doi.org/10.1021/es301294q>
- Ruf, M., & Steeb, H. (2020). An open, modular, and flexible micro X-ray computed tomography system for research. *Review of Scientific Instruments*, 91(11), 113102. <https://doi.org/10.1063/5.0019541>
- Vahid Dastjerdi, S., Steeb, H., Ruf, M., Lee, D., Weinhardt, F., Karadimitriou, N., & Class, H. (2021). Micro-XRCT dataset of Enzymatically Induced Calcite Precipitation (EICP) in a microfluidic cell. *DaRUS*. <https://doi.org/10.18419/darus-866>
- van Paassen, L. (2009). *Biogrout: Ground improvement by microbially induced carbonate precipitation* (PhD thesis). Delft, the Netherlands: Delft University of Technology.
- van Paassen, L., Ghose, R., van der Linden, T., van der Star, W., & van Loosdrecht, M. (2010). Quantifying biomediated ground improvement by ureolysis: Large-scale biogrout experiment. *Journal of Geotechnical and Geoenvironmental Engineering*, 136(12), 1721–1728. [https://doi.org/10.1061/\(ASCE\)GT.1943-5606.0000382](https://doi.org/10.1061/(ASCE)GT.1943-5606.0000382)
- Wang, Y., Soga, K., Dejong, J. T., & Kabla, A. J. (2019). A microfluidic chip and its use in characterising the particle-scale behaviour of microbial-induced calcium carbonate precipitation (MICP). *Géotechnique*, 69(12), 1086–1094. <https://doi.org/10.1680/jgeot.18.P.031>
- Weinhardt, F., Class, H., Vahid Dastjerdi, S., Karadimitriou, N., Lee, D., & Steeb, H. (2021). Optical microscopy and pressure measurements of Enzymatically Induced Calcite Precipitation (EICP) in a microfluidic cell. *DaRUS*. <https://doi.org/10.18419/darus-818>
- Wiffin, V., van Paassen, L., & Harkes, M. (2007). Microbial carbonate precipitation as a soil improvement technique. *Geomicrobiology Journal*, 24(5), 417–423. <https://doi.org/10.1080/01490450701436505>
- Xia, Y., & Whitesides, G. M. (1998). Soft lithography. *Angewandte Chemie International Edition*, 37(5), 550–575. <https://doi.org/10.1146/annurev.matsci.28.1.153>
- Yoon, H., Valocchi, A. J., Werth, C. J., & Dewers, T. (2012). Pore-scale simulation of mixing-induced calcium carbonate precipitation and dissolution in a microfluidic pore network. *Water Resources Research*, 48, W02524. <https://doi.org/10.1029/2011WR011192>
- Zhang, C., Dehoff, K., Hess, N., Oostrom, M., Wietsma, T. W., Valocchi, A. J., et al. (2010). Pore-scale study of transverse mixing induced CaCO₃ precipitation and permeability reduction in a model subsurface sedimentary system. *Environmental Science & Technology*, 44(20), 7833–7838. <https://doi.org/10.1021/es1019788>